Optimizing mechanostable anchor points of engineered lipocalin in complex with CTLA-4

Zhaowei Liu[1, 2], Rodrigo A. Moreira[3], Ana Dujmović[1,2], Haipei Liu[1,2], Byeongseon Yang[1,2], Adolfo B. Poma[3] and Michael A. Nash[*, 1, 2]

[1] Institute of Physical Chemistry, Department of Chemistry, University of Basel, 4058 Basel, Switzerland

[2] Department of Biosystems Science and Engineering, ETH Zurich, 4058 Basel, Switzerland

[3] Biosystems and Soft Matter Division, Institute of Fundamental Technological Research, Polish Academy of Sciences, Pawińskiego 5B, 02-106 Warsaw, Poland

*Correspondence to: michael.nash@bsse.ethz.ch

Abstract

Anticalin is a non-antibody protein scaffold with potential as an alternative to monoclonal antibodies for targeted drug delivery to cytotoxic T-lymphocyte antigen 4 (CTLA-4) positive T-cells. In this context, one limiting factor is the ability of the anticalin:CTLA-4 complex to resist mechanical forces exerted by local shear stress. Here, we used single-molecule AFM force spectroscopy (AFM-SMFS) to screen residues along the anticalin backbone and determine the optimal anchor point that maximizes binding strength of the anticalin:CTLA-4 complex. We used non-canonical amino acid incorporation by amber suppression combined with click chemistry to attach an Fgβ peptide at internal residues of the anticalin. We then used Fgβ as a handle to pick up and mechanically dissociate anticalin from CTLA-4 from eight different anchoring residues using an AFM cantilever tip. By quantifying the unbinding energy landscape for each pulling geometry, we found that pulling on the anticalin from residue 60 or 87 resulted in significantly higher rupture forces and a decrease in k_{off} by 2-3 orders of magnitude over a force range of 50-200 pN. Five of the six internal pulling points tested were significantly more stable than N- or C-terminal anchor points, rupturing at up to 250 pN at loading rates of 0.1-10 nN sec^{-1}. Anisotropic network modelling, along with molecular dynamics (MD) simulations using the Gō-MARTINI approach explain the mechanism underlying the geometric dependency of mechanostability. These results suggest that optimization of attachment residue position for therapeutic and diagnostic cargo can provide large improvements in binding strength, allowing affinity maturation without requiring genetic mutation of binding interface residues.

Introduction

Next-generation biotherapeutics are moving beyond full length IgG antibodies and into the realm of non-antibody scaffolds. Compared to conventional monoclonal antibodies, non-antibody scaffolds are smaller in size, easier to manufacture and can exhibit low immunogenicity, making them attractive as diagnostic tools and drug carriers[1,2]. Scaffolds such as anticalins, DARPins and adnectins can be diversified at the genetic level and evolved *in vitro* to bind many different molecular targets[3].

Anticalins are a class of non-antibody scaffolds derived from naturally occurring lipocalins[4]. The anticalins share homologous backbone structures (**Fig. S1**), but their ligand binding loops are engineered to specifically bind diverse molecular targets, including proteins, peptides and small molecules[5–10]. Among these targets, human cell surface receptors that are overexpressed in tumors or immune cells are of particular interest. Cytotoxic T-lymphocyte antigen 4 (CTLA-4) is involved in negative regulation of T-cell immune function and maintenance of immune homeostasis[11,12]. Certain tumors are able to take advantage of immune checkpoints including CTLA-4 to escape the immune system[13,14], and blockage of CTLA-4 through binding of inhibitory antibodies or non-antibody scaffolds can help improve efficacy of antitumor therapies[15,16], therefore CTLA-4 represents an important target for tumor immunotherapy[17]. One important approach in targeted drug delivery and diagnostic *in vivo* imaging is based on coating nanoparticles with affinity proteins to target them to specific cell types[18–20]. In this context, non-antibody scaffolds are used for recognizing the target cells and mediating adhesion between nanoparticles and cells, and a limiting factor is the binding strength of the non-antibody scaffold:ligand complex.

It is well appreciated that the force required to mechanically denature a protein is highly dependent on the pulling geometry[21–24]. By pulling geometry we refer to the precise amino acid positions through which mechanical tension is applied to a folded protein domain or a protein-protein complex. Different geometries give rise to diverse intramolecular force propagation pathways and thus significantly affect the unbinding or unfolding energy landscape. In the case of protein-protein complexes, cohesin-dockerin and monovalent streptavidin (mSA)-biotin systems have considerably diverse responses to external forces when loaded from the N- vs. C- terminus[25,26]. The mechanical stability of biotin:streptavidin complexes is also known to be dependent on the loading geometry[27]. Currently it remains unclear precisely how pulling geometry modulates the binding strength of protein-protein complexes. If there were generalizable principles by which to design and optimize loading geometries, this information could help in the development of improved non-antibody scaffolds for targeted therapeutics and *in vivo* imaging probes.

Single-molecule force spectroscopy with atomic force spectroscope (AFM-SMFS) is a powerful tool to study the force response of protein-protein complexes. State-of-the-art AFM setups are able to precisely control the pulling geometry of receptor-ligand systems and measure a wide range of forces[28–30]. Here, we used AFM-SMFS to study the response of anticalin:CTLA-4 complexes to external forces under different loading geometries. We systematically scanned the anchoring residue on anticalin

from the N- to the C-terminus, targeting flexible loop regions located between secondary structural elements, and quantified the unbinding energy landscape for each anchor point. Our experimental approach was combined with molecular dynamics (MD) simulations, which showed consistency with the experimental results and helped us gain mechanistic insight into the unbinding pathways of the anticalin:CTLA-4 complex under different loading geometries.

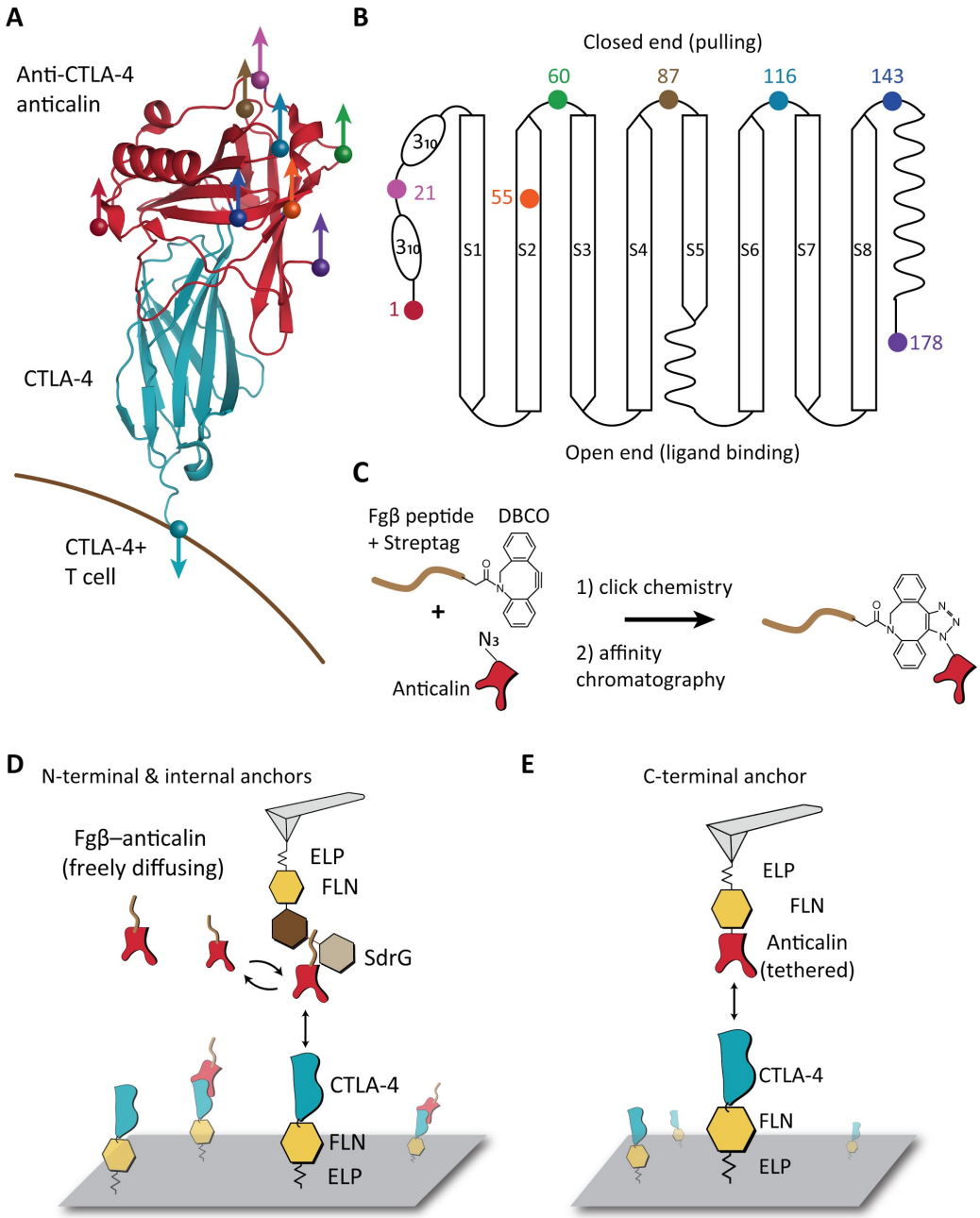

Figure 1. Anchor point selection and AFM-SMFS measurement setups. A: Structure of CTLA-4 in complex with anticalin (PDB code 3BX7). Anchor points on the anticalin are shown as colored spheres. The anchor point on CTLA-4 is fixed at the C-terminus, mimicking the natural tethering geometry on the cell surface. **B:** Anticalin has a central β-barrel, consisting of eight anti-parallel β-strands (S1-S8) connected by short flexible linkers. The anchor points shown as colored dots were chosen at the closed end of the β-barrel to avoid interference with the binding interface. **C:** Bioorthogonal conjugation of a

fibrinogen β (Fgβ) peptide to the anticalin. The residue at the selected anchor point was replaced by p-azido-phenylalanine using amber suppression to introduce an azide group. The azide was covalently linked with a synthetic peptide comprising Fgβ-StrepTag and a C-terminal DBCO group using click chemistry. **D:** AFM measurement setup for testing N-terminal and internal anchor points with freely diffusing Fgβ-anticalin. Anticalin conjugated with Fgβ was added to the measurement buffer to final concentration of 1 μM. SdrG-FLN-ELP-ybbr was immobilized on the AFM tip and the ligand (CTLA-4-FLN-ELP-ybbr) was immobilized on the glass surface covalently via ybbr tag. **E:** AFM measurement setup with tethered anticalin for probing C-terminal anticalin anchor point. Anticalin-FLN-ELP-ybbr was immobilized on the cantilever and CTLA4-FLN-ELP-ybbr was immobilized on the glass surface.

Results

Selection of anchor points, protein expression and AFM measurement setup

The anticalin targeting CTLA-4 was derived from human neutrophil gelatinase-associated lipocalin (NGAL). The structure of anticalin in complex with the extracellular domain of CTLA-4 is shown in **Fig. 1A** (PDB code 3BX7)[5]. CTLA-4 is a human T cell receptor with the C-terminus of the extracellular domain anchored to the cell surface. As shown in **Fig. S1**, the structure of anticalin is highly homologous to other previously reported lipocalin folds[10,31–34], comprising a β-barrel formed by eight anti-parallel β-strands, flanked by helical regions at the N- and C-termini[35,36]. The two ends of the barrel are the open end, which is involved in ligand binding, and the closed end. Based on the protein structure, we selected eight anchor points on anticalin, scanning the sequence length through eight different pulling geometries. These anchor points were the N- and C- termini (residues 1 and 178), five residues located along flexible linkers connecting the β-strands (residues 21, 60, 87, 116 and 143), and one located within β-strand S2 (residues 55). All of the internal anchor points were located at the closed end of the barrel (**Fig. 1A and B**). N- and C- terminal anchor points were towards the open end of the barrel closer to the bound CTLA-4 ligand.

Each anchor point on the anticalin molecule corresponds to a precisely defined pulling geometry in the AFM measurements. In order to attach the internal anchor points (residues 21, 55, 60, 87, 116 and 143) to the AFM tip, we combined non-canonical amino acid (NCAA) incorporation, click chemistry and a recently-reported AFM-SMFS setup with freely diffusing receptor molecules[26,30]. As shown in **Fig. 1C**, the residue at the selected anchor point was replaced by a p-azido-L-phenylalanine using amber suppression to introduce an azide group[37] during protein translation in *E. coli*. A synthetic peptide comprising N-terminus fibrinogen β (Fgβ) peptide, Strep-tag and C-terminus dibenzocyclooctyne (DBCO) group was subsequently conjugated with the azide group on the anticalin using copper-free click chemistry[38]. The reaction product was purified with size-exclusion and Strep-trap columns to remove excess peptide and unreacted anticalin. Successful conjugation of the peptide increased the molecular weight of anticalin by 3 kD, as confirmed by SDS-PAGE and mass

spectrometry (**Fig. S2**). Each anticalin with Fgβ clicked onto a given residue was expressed and purified, and measured in separate AFM experiments.

The AFM experimental setup with freely diffusing anticalin is shown in **Fig. 1D**. CTLA-4 was cloned to the N-terminus of a polyprotein, followed by an FLN unfolding fingerprint domain[39], an elastin-like peptide (ELP) elastic linker, and a ybbr tag at the C-terminus. The ybbr tag facilitated site-specific and covalent surface immobilization of the polyprotein[40] to the glass surface. The C-terminus of CTLA-4 was tethered to the glass surface, mimicking the natural pulling geometry on the cell surface. SD-repeat protein G (SdrG) from *S. epidermidis* which binds Fgβ was cloned into the polyprotein SdrG-FLN-ELP-ybbr and immobilized on the AFM tip.

The anticalin with Fgβ peptide conjugated to the selected anchor point was added to the measurement buffer to final concentration of ~1 μM, which saturated immobilized CTLA-4 on the surface. SdrG on the cantilever can bind and unbind with Fgβ-anticalin in solution. A significant portion of the time, SdrG on the cantilever is free and when it approaches the surface, a 3-member complex forms, consisting of cantilever-borne SdrG bound to Fgβ-anticalin, which was itself in turn bound to CTLA-4. Alternatively, if SdrG was occupied by an Fgβ-anticalin molecule when the cantilever approached and indented the surface, mechanical contact can stimulate Fgβ ligand exchange, allowing the same 3-member complex to form. If no such exchange occurs, the AFM trace results in no specific interactions being recorded.

Despite the rapid on/off exchange of SdrG:Fgβ complexes at equilibrium, when placed under tension these complexes are extremely mechanically stable and can withstand forces as high as 2 nN [41]. When retracting the cantilever the significantly weaker anticalin:CTLA-4 complex was therefore the first to break, leaving the Fgβ conjugated anticalin on the cantilever. Since the affinity between SdrG and Fgβ is mediocre (Kd ~400 nM)[42], the anticalin on the cantilever quickly exchanged with the freely diffusing anticalin molecules in the solution, preventing the AFM tip from clogging[26]. Tens of thousands of approach-retract cycles could be performed in this format repeatedly using a range of constant pulling speeds from 100 nm s^{-1} to 800 nm s^{-1} to build up large statistics. In this measurement format, it is important to note that the cantilever and surface molecules are always freshly probed, so the refoldability of the cantilever-borne molecules does not play a role.

For the N-terminal anchor point, anticalin was cloned and expressed with the Fgβ peptide at its N-terminus and measured using the freely diffusing setup. However, since the SdrG:Fgβ complex is itself directionally dependent, it was not possible to use Fgβ as a C-terminal anchor point. To anchor the anticalin from the C-terminus, we used an AFM setup with tethered anticalin, where a polyprotein containing anticalin at the N-terminus (anticalin-FLN-ELP-ybbr) was directly immobilized on the cantilever, as shown in **Fig. 1E**. The protocol for AFM cantilever approaching, dwelling and retracting was kept the same as for the setup with freely diffusing anticalin.

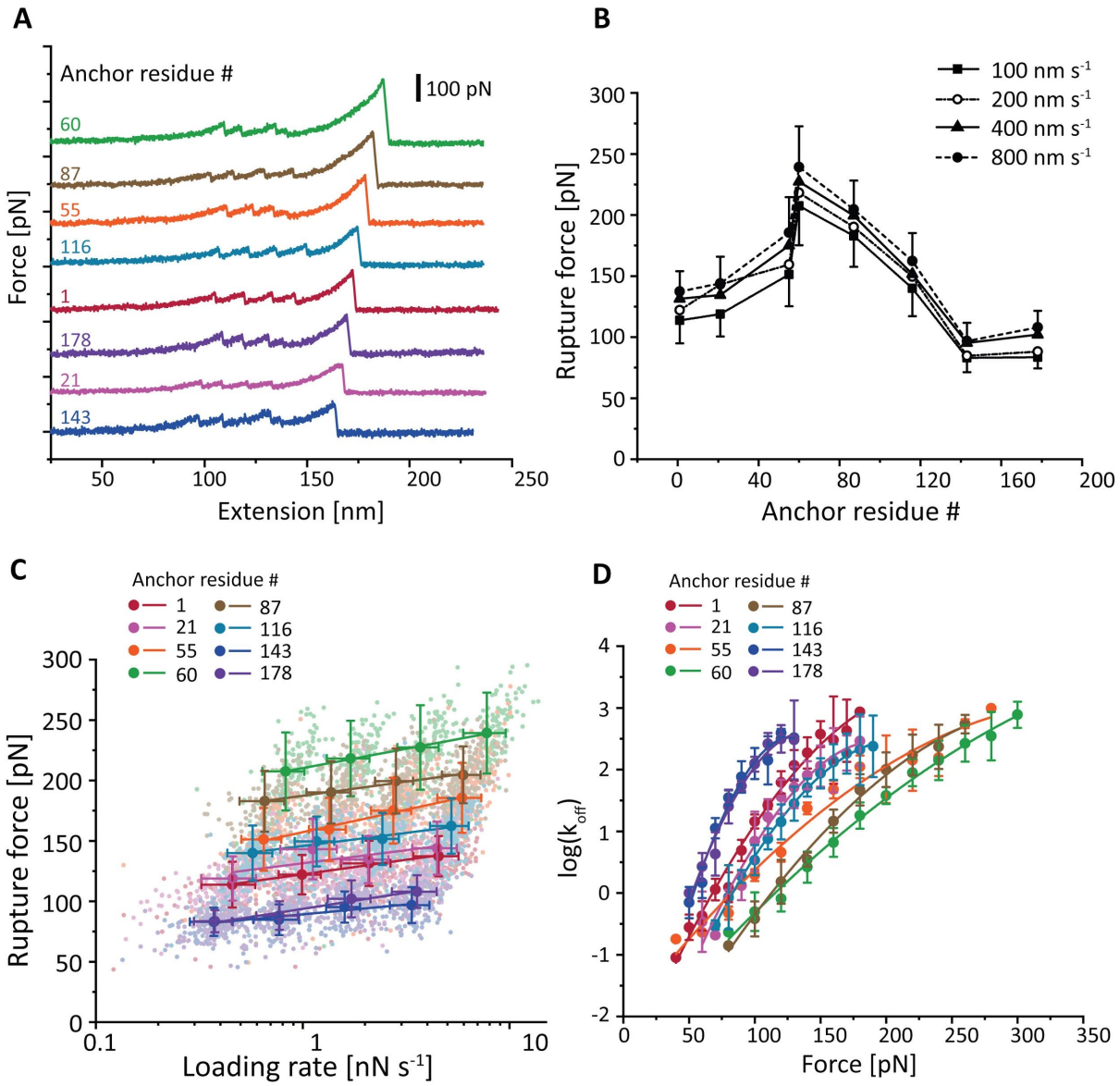

Figure 2. Dependency of anticalin:CTLA-4 complex stability on anticalin anchor position. A: Example AFM force-extension traces measured with eight different pulling geometries. Each trace shows unfolding of 2 FLN fingerprint domains and rupture of the anticalin:CTLA-4 complex for a given anchor residue on anticalin. **B:** Most probable rupture forces of the anticalin:CTLA-4 complex at various pulling speeds were plotted against the anchor residue number on anticalin. Error bars represent standard deviation of rupture forces measured at 100 nm s^{-1} (minus) and 800 nm s^{-1} (plus) pulling speeds. **C:** Most probable rupture forces measured at different pulling speeds were plotted against the logarithm of average loading rate and fitted linearly to extract the zero-force off rate k_0 and distance to the transition state $\Delta x^{\ddagger}$. Error bars represent the standard deviation of rupture forces and loading rates. **D:** Force-dependent off rate of anticalin:CTLA-4 complex was plotted against force and fitted using Eq. 6 to extract k_0, $\Delta x^{\ddagger}$ and $\Delta G^{\ddagger}$. Error bars represent the standard deviation of off rates measured at four different pulling speeds.

Different pulling geometries gave rise to diverse unbinding energy profiles

In a typical AFM measurement (~12 h), around 10,000 force-extension curves were recorded and transformed into contour length space using a freely rotating chain (FRC) elasticity model[43]. The curves were filtered based on the two-step unfolding pattern and 32 nm contour length increment of two FLN fingerprint domains[39]. In both AFM setups with freely diffusing or tethered anticalin, one FLN was on the cantilever and another was on the cover glass. We only analyzed the curves containing two FLN unfolding events to rule out nonspecific interactions and multiple parallel interactions between the tip and glass surface. Example force-extension curves of different pulling geometries are shown in **Figs. 2A and S3**. Intermediate unfolding events were observed in ~9% of selected force curves, including all eight pulling geometries (**Fig. S3**). We aligned the contour length histograms of all the selected curves using cross-correlation analysis. The resulting superposition histogram (**Fig. S4**)[44,45] showed contour length increments corresponding to the two FLN domains, which together added 64 nm of additional contour length to the system.

Rupture forces of the anticalin:CTLA-4 complex for each Fgβ anchoring residue number were measured in separate AFM data collection runs at four different pulling speeds ranging from 100 to 800 nm s^{-1}. The forces required to dissociate anticalin from CTLA-4 were plotted as histograms, as shown in **Fig. S5**. The histograms were fitted to extract the most probable rupture forces, which were plotted against the anchor residue number on anticalin (**Fig. 2B**). It is clear from the plot that the mechanical stability of the anticalin:CTLA-4 complex is highly dependent on the anticalin anchor residue number. N- and C-terminal pulling points were among the lowest in stability, rupturing at 100-125 pN. The stability significantly rose for anchor points located near the middle of the protein sequence, for example at residues 60 and 87. Peak stability (~225 pN) was achieved when anticalin was anchored at residue 60, between β-strands S2 and S3.

We used Bell-Evans (BE)[46,47] and Dudko-Hummer-Szabo (DHS)[48,49] models to extract the unbinding energy profile parameters for each pulling geometry. As shown in **Fig. 2C**, the rupture forces measured at each pulling speed were plotted against the logarithm of loading rate, and the most probable rupture forces were linearly fitted against the average loading rate at a given pulling speed to extract the zero force off-rate (k_0) and the distance to the energy barrier ($\Delta x^{\ddagger}$) using the BE model. We next used the DHS model (**Fig. 2D**) to transform the rupture force histograms into force-dependent off-rates (Eq. 4), and fitted the resulting plot using Eq. 6 to obtain the k_0, $\Delta x^{\ddagger}$ and the height of the energy barrier ($\Delta G^{\ddagger}$). The k_0, $\Delta x^{\ddagger}$ and $\Delta G^{\ddagger}$ values obtained using both models are listed in **Table 1**.

It is clear from **Fig. 2** and **Table 1** that the complex crossed unbinding energy barriers with significantly different heights and shapes when pulled from different anchor points. Depending on the anchor residue number, the kinetic off-rate k_{off} at a given force can vary by 2-3 orders of magnitude (**Fig. 2D**, 100 pN). Both DHS and BE models extracted short $\Delta x^{\ddagger}$ values for anchor residue 60 (DHS: 0.25 ± 0.02 nm; BE 0.30 ± 0.01 nm) indicating a short steep energy barrier when tension was applied through the middle of the beta barrel on anticalin.

Analysis with anisotropic network model

To help interpret our experimental observations, we applied an anisotropic network model (ANM) to calculate the effective spring constant between different pairs of residues[50,51] in the protein complex. The ANM has been previously applied to several isolated protein domains including α-amylase inhibitor, green fluorescence protein (GFP), human ubiquitin and *E. coli* pyruvate dehydrogenase (PDH) E2lip3 domain, and the results were compared with MD simulations and experimental data[52,53]. Here we applied the ANM to the anticalin:CTLA-4 complex and derived effective spring constants between pairs of residues located on separate chains within the crystal structure. One residue was held fixed at the C-terminus of CTLA-4 while the other was scanned through all the residues on anticalin **(Fig. S6)**. To compare the predicted force constants from the ANM with the rupture forces and energy landscape parameters, we focused on the eight anchor residues on anticalin which were experimentally measured by AFM-SMFS **(Table S1)**. As shown in **Fig. S7**, the correlation between the experimentally measured rupture forces and the effective spring constant is not significant ($p = 0.42$). However, the k_0 parameter derived using the DHS model, along with the $\Delta x^{\ddagger}$ value derived from the BE model were both statistically correlated ($p < 0.05$) with the effective spring constants between pairs of residues predicted by the ANM. The $\Delta G^{\ddagger}$ parameter derived from the DHS model was weakly correlated ($p = 0.07$). Both $\Delta G^{\ddagger}$ (DHS) and $\Delta x^{\ddagger}$ (BE and DHS) increased with increasing effective force constant, while k_0 (DHS model) decreased with increasing effective force constant. The k_0 calculated using the BE model, however, had negligible correlation with the effective force constant. We note that the unbinding energy profile measured for anticalin anchored from residue 55 was considered an outlier and excluded from the aforementioned correlation analysis. Residue 55 is the only anchor point located in a rigid region (β-strand) of anticalin. All other anchor residues are located at termini or within flexible loops. Due to its comparatively high structural rigidity, position 55 gave rise to the highest effective spring constant predicted by ANM, and resulted in a unique unbinding energy profile with a medium to low energy barrier and short $\Delta x^{\ddagger}$. Excluding residue 55, several of the experimentally determined energy landscape parameters were statistically correlated with the effective spring constant determined by the ANM approach. These findings provide evidence that ANM can be used to predict the anisotropic mechanical properties of protein-protein complex binding interfaces **(Figs. S6 and S7)**.

Table 1. Unbinding energy landscape parameters of the anticalin:CTLA-4 complex under different pulling geometries.

Anchor point on anticalin	k_0 [s^{-1}] (DHS)	k_0 [s^{-1}] (BE)	$\Delta x^{\ddagger}$ [nm] (DHS)	$\Delta x^{\ddagger}$ [nm] (BE)	$\Delta G^{\ddagger}$ [k_BT] (DHS)
1	$(1.0\pm0.5)\times10^{-3}$	$(8\pm5)\times10^{-4}$	0.50±0.05	0.40±0.03	16.8±0.6
21	$(7\pm9)\times10^{-5}$	$(1\pm7)\times10^{-4}$	0.63±0.09	0.4±0.2	18±1
55	$(9\pm6)\times10^{-3}$	$(4\pm3)\times10^{-3}$	0.27±0.04	0.26±0.02	13.9±0.9
60	$(2\pm1)\times10^{-3}$	$(2\pm1)\times10^{-5}$	0.25±0.02	0.30±0.01	17±1
87	$(2\pm1)\times10^{-4}$	$(1\pm1)\times10^{-6}$	0.38±0.03	0.41±0.03	17.8±0.4
116	$(1.0\pm0.3)\times10^{-4}$	$(2\pm4)\times10^{-5}$	0.57±0.02	0.44±0.07	17.2±0.2
143	$(4\pm5)\times10^{-5}$	$(0.4\pm1)\times10^{-3}$	1.0±0.1	0.6±0.1	18±1
178	$(2\pm2)\times10^{-4}$	$(3\pm2)\times10^{-2}$	0.8±0.1	0.36±0.04	17±1

Utilizing experimental data to improve hybrid all-atom and Gō-MARTINI descriptions of protein binding interfaces

Next we analyzed the anticalin:CTLA-4 system using a structure-based coarse grained model that combined the MARTINI force field[54,55] with a Gō-like description of all native contacts that maintain secondary and tertiary structures in the protein. The latter model has been used in previous studies on mechanical stability of single protein domains[56–58] and protein aggregates[59–61]. Combined Gō-MARTINI now allows analysis of large conformational changes in proteins, and the characterization of protein mechanical properties[62,63]. Gō-MARTINI simulations of anticalin:CTLA-4 dissociation under different pulling geometries at first failed to reproduce the rupture force profile as a function of residue position as obtained by SMFS (**Fig. S8**). This indicated an incomplete representation of the energetics at the interface, a known issue in MARTINI force fields[64]. Hence, an additional set of native contacts (NCs) obtained from the crystal structure (PDB code 3BX7) were included in the Gō-MARTINI model to better describe the binding interface between anticalin and CTLA-4 (**Fig. S8A**) using Gō contact map determination (http://pomalab.ippt.pan.pl/GoContactMap/). However, this minimal description of contacts was again insufficient to capture the experimental SMFS profiles (**Fig. S8B**). To provide qualitative agreement with experiments and remain consistent with a minimal representation of the binding interface dictated by structure, an additional native contact was introduced.

This contact was chosen through a systematic process considering contacts established within a cutoff distance equal to 0.9 nm between any pair of Cα-atoms laying at the interface. Then, we performed pulling simulations for each of them to identify the one which improved the rupture profile. Thus, an additional contact between PRO102 (CTLA-4) and VAL66 (anticalin) was included in the contact map (CM). The updated CM improved the energetic description of the protein-protein interface and could be tuned to achieve simulations that reproduced the experimental rupture force profiles (**Fig. S8B**). In order to map the energetics of the all-atom MD simulation for the interface, the energy of the additional contact was tuned to reproduce atomistic energy in equilibrium. This step corrects the energy scale of the protein-protein interface via an energy parameter (ε_{core}). Note that the standard native contact energy ($\varepsilon_{Gō\text{-}MARTINI}$) is equal to 9.414 kJ mol^{-1} in the Gō-MARTINI model. The ε_{core} parameter was incrementally increased, and the system was evaluated via pulling simulations at different residue positions until the rupture force profile reached a qualitative agreement with the experiments (SMFS data from **Fig. 2B**). The corresponding value of ε_{core} that allowed this reconciliation was achieved at ε_{core} = 100 kJ mol^{-1} (see **Fig. S8B**). This result was validated in an ensemble (n=100) of different pulling simulations (see **Fig. S9**) for each anchor point. Although the optimal ε_{core} value is an order of magnitude larger than $\varepsilon_{Gō\text{-}MARTINI}$, its value is bounded by the typical energy scales we found in all-atom MD simulation. The energetic decomposition for the anticalin:CTLA-4 complex allows us to verify the improvement given by the Gō-MARTINI description. **Table S2** shows the energy values for each protein chain and the protein-protein interface, which was defined by amino acid residues that form contacts between CTLA-4 and anticalin in the native structure. On average the energy at the interface in all-atom MD corresponded to 4% of total energy. The same decomposition for the Gō-MARTINI model assigned an average value of about 6% of the total energy. Note that our model retains the energy ratio for CTLA-4 and anticalin in good agreement with all-atom MD. The stability of the anticalin:CTLA-4 complex is mediated by the stability of the interface. The number of NCs was 189, 275 and 33 NCs for CTLA-4, anticalin and the protein-protein interface during 100 ns MD simulation.

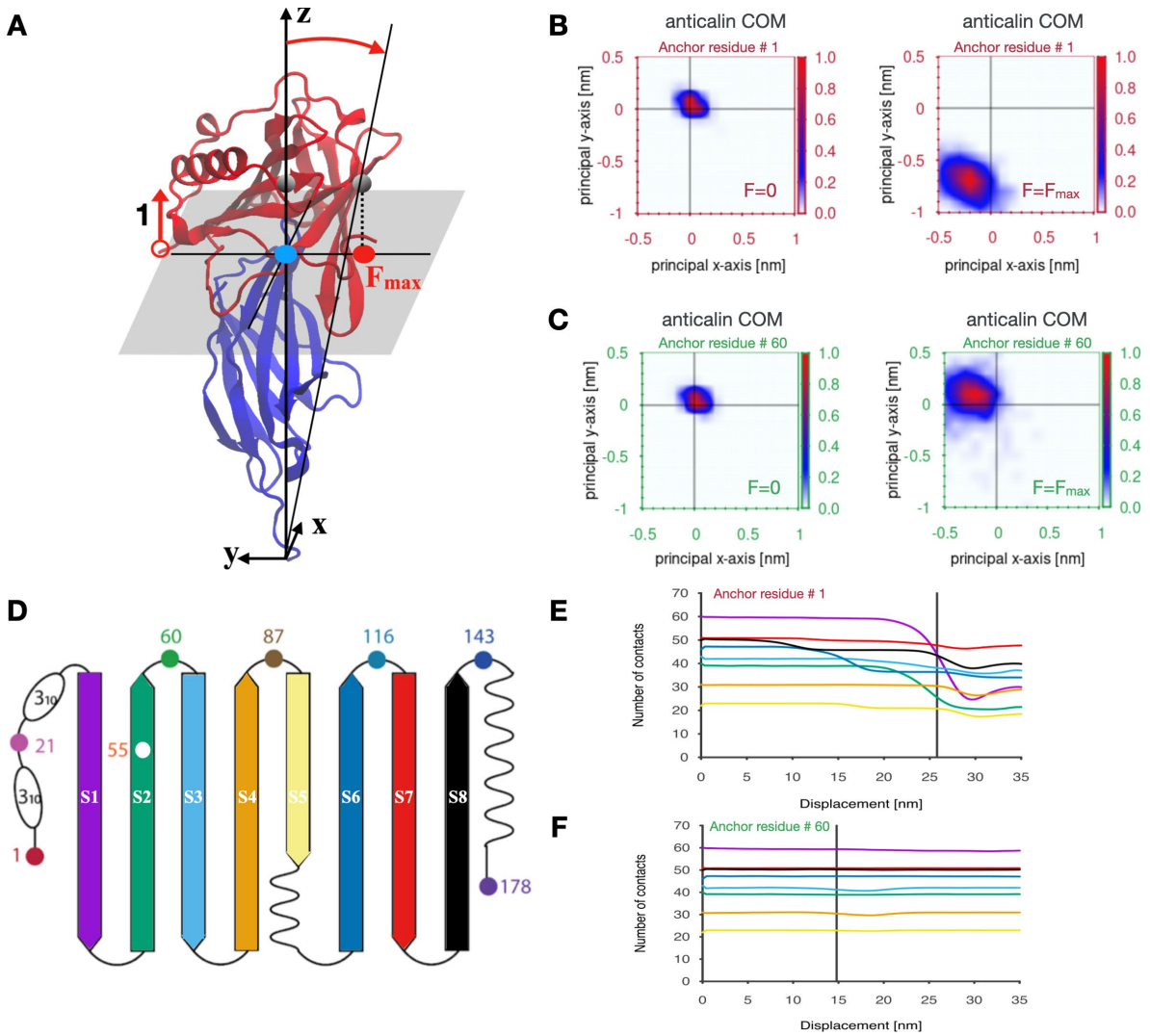

Figure 3. Molecular characterization of Gō-MARTINI trajectory for anticalin:CTLA-4 complex at different pulling geometries. A: The translation of anticalin COM for anchor residue 1 under a force applied along the z direction. The CTLA-4 was used as a reference system to define the normal plane. Blue circle denotes the starting anticalin COM position and the red one its translation along -y direction at F_{max}. **B and C**: The relative translation of the anticalin COM with respect to CTLA-4 molecule for two anticalin anchor residues 1 **(B)** and 60 **(C)** at F = 0 and F = F_{max}. Color bars indicate the probability of finding the COM in a given position along the X-Y plane which is perpendicular to the z direction of symmetry of the complex. **D:** The beta-sheet structure of the anticalin and its color representation. **E and F:** The intrachain native contact (NC) evolution for anticalin computed for each beta-sheet during the pulling process. Severe loss of contacts affects the anticalin for the pulling residue 1, whereas almost no loss of NC is reported for anchor residue 60. Color line is in agreement with the panel D.

Calibrated Gō-MARTINI model provides molecular insights into deformation pathways

With the calibrated model established, we next analyzed the trajectories to help explain the observed differences in binding strength as a function of anchor point. The first analysis we carried out was to monitor the position of the center-of-mass (COM) of anticalin during the pulling simulations (see **Fig. 3A**). **Fig. 3BC** compare the COM position of anticalin at zero force and at the maximal force observed in the simulation (F_{max}) for anticalin anchor residues 1 (low stability) and 60 (high stability). For anchor residue 1, at F_{max} the COM of anticalin was clearly shifted in the negative y-direction by ~0.75 nm and in the negative x-direction by ~0.2 nm. However, when pulling anticalin from residue 60, the anticalin COM stayed close to its original position, translating slightly in the positive y-direction (~0.1 nm) and negative x-direction (~0.2 nm). These differences suggest a scenario where pulling from the N-terminus results in a peeling-like behavior of anticalin off of CTLA-4, while pulling from position 60 results in a well-aligned system that cooperatively breaks without translating. Analysis of the xy translation of anticalin COM was carried out for each anchor residue under pulling simulations (**Fig. S10**). These plots show that COM translation behavior is distinct for each anchor point. The lowest stability anchor point tested experimentally (residue #143) also shows a broad distribution of translation values for anticalin COMs at F_{max} suggesting significant deformation of the complex and rearrangement under tension.

The second MD analysis we carried out was to analyze the number of NCs (**Fig. 3EF and Fig. S11**) lost in different regions of anticalin when it was pulled from different directions. When pulling from residue 1, NCs were steadily lost in N-terminal beta strands S1, S2, S3 as well as S6 prior to rupture. However, when pulling from residue 60, few to no intramolecular NCs were lost in the anticalin (**Fig. 3F**). The anticalin COM shift is more pronounced when several anticalin beta-sheets lose some of the stabilizing NCs (**Fig. S11**). Our analysis of the intrachain NCs suggest that breaking NCs in the beta strands makes the anticalin more flexible and its COM samples new positions through different pathways. Furthermore, pathways involving partial unfolding processes and severe loss of NCs were observed for anchor residues 1 and 21 (**Fig. S11**). The NCs on the binding interface also behave differently depending on the pulling geometry (**Table S3 and Fig. S12**). The interface NCs were lost at different rates with different pulling geometries and the number of remaining interface NCs at F_{max} (immediately prior to rupture) varies across the simulations and shows positive correlation ($p<0.05$) with the rupture force measured both *in vitro* and *in silico* (**Fig. S13**). In addition, a few non-native contacts (about five, see **Fig. S12**) are established after the rupture. However, the new protein-protein interactions established during the dissociation pathway are not strong enough to maintain the mechanical stability of anticalin:CTLA-4 complex. Based on the simulation analyses, we conclude that the persistence of the original set of interface NCs, the translation of the anticalin COM and the loss of beta strand structure explain the geometric dependency of the mechanical properties of the complex.

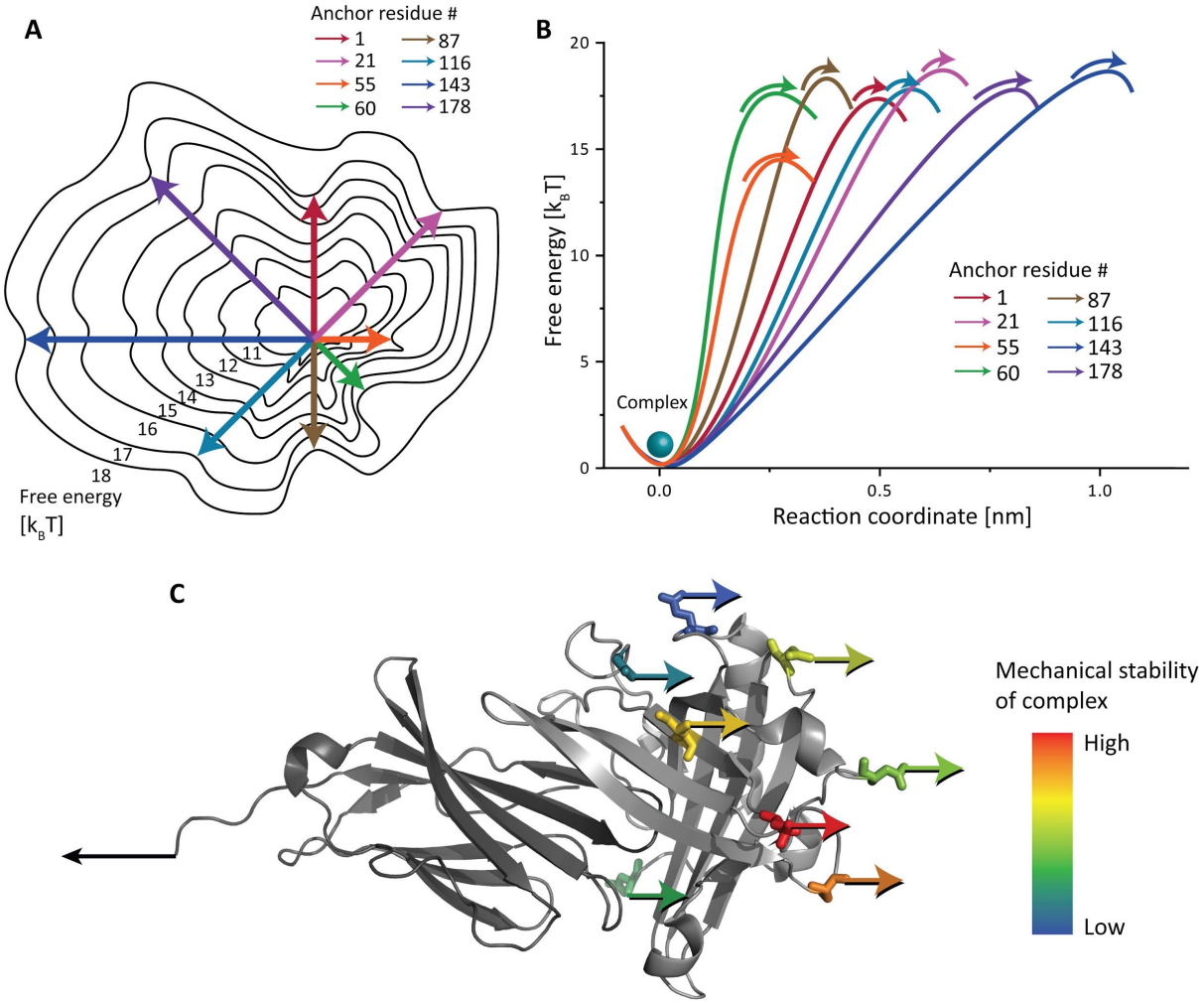

Figure 4. Depictions of anticalin:CTLA-4 complex unbinding energy landscape as a function of molecular pulling geometry. A: Energy landscape depiction where anchor point residues are represented as cardinal and ordinal directions of a compass. Under a constrained pulling geometry, the complex is forced to traverse different unbinding pathways across the energy landscape. These different paths give rise to energy barriers with diverse heights and shapes. **B:** 1D depiction of unbinding energy barrier heights and positions calculated using the DHS model for each pulling geometry (see **Table 1**). **C:** Anchor points on the anticalin colored based on mechanical stability of the complex pulled through that position. The most and least mechanostable anchor points on the anticalin are residues 60 (red) and 143 (dark blue), respectively.

Discussion

Here, we reported a novel AFM-SMFS experimental method to covalently click a mechanostable peptide handle to internal residues of the non-antibody scaffold anticalin/lipocalin and to measure the rupture forces of anticalin:CTLA-4 complexes using an AFM setup with freely diffusing molecules. Using this method, we observed how the anticalin:CTLA-4 complex responds to external forces applied from different directions and found that the mechanical stability of the complex is highly

dependent on the pulling geometry. When pulling from anticalin residue 60, the complex could withstand a high force up to 200 pN, which is ~100% higher than the least mechanically stable pulling geometry (residue 143). To confirm that the different constructs have similar equilibrium affinity, we measured the dissociation constant between CTLA-4 and three anticlain mutants using microscale thermophoresis (MST). As shown in **Table S4**, although the anticalin E60AzF and E143AzF mutants have distinct responses to forces when pulled from different geometries, they have similar affinity towards CTLA-4 at equilibrium. The exception is the I55AzF mutant, which has a slightly lower affinity with CTLA-4. The anticalin mutants were conjugated with a bulky molecule using DBCO-azide reaction in both SMFS (with Fgβ peptide) and MST (with AF647 dye) measurements. Since residue 55 is on a β-strand, which is a part of the anticalin β-barrel structure, the mutation to pAzF and conjugation of peptide or fluorescent dye may have slightly destabilized the anticalin:CTLA-4 complex. Therefore, the I55AzF mutant gave rise to a lower energy barrier in SMFS measurement (see **Table 1** and **Fig. S7**) as well as lower equilibrium affinity in bulk experiments compared to other anticalin constructs.

Fig. 4AB illustrates the complex dissociation energy landscape. In the absence of force, the complex has the same free energy in different pulling geometry scenarios. When external force is applied to the complex from different anchor points, the complex unbinds through different pathways. These pathways correspond to unbinding energy barriers with different shapes and heights, giving rise to distinct responses to forces. It is worth noting that the energy barrier of the most mechanostable pulling geometry (anchor residue 60) is not the highest, but its exceptionally short $\Delta x^{\ddagger}$ contributed to the high resistance to external force. On the contrary, although the pulling geometry with anchor residue 143 has the highest energy barrier, the long $\Delta x^{\ddagger}$ made it the least mechanostable pulling geometry. Another interesting pulling geometry, anchor residue 55, has a unique energy landscape with the lowest energy barrier and a short $\Delta x^{\ddagger}$, giving rise to a mediocre rupture force among all pulling geometries. Therefore, the mechanical stability of the complex is determined by an interplay between the height and the shape of unbinding energy barriers.

We further used the anisotropic network model (ANM) to calculate the force constant between the eight anchor residues on the anticalin and the C-terminal anchor point of CTLA-4. While the effective force constant has very weak correlation with the rupture force, it is correlated with many of the energy profile parameters calculated using both Bell-Evans and Dudko-Hummer-Szabo models. However, residue 55 of anticalin, which is located on a rigid β strand while all the other anticalin anchor points are at the termini or in flexible loops, is an outlier in all of these correlations. This indicates that the AMN approach has certain limitations and additional factors, for example secondary structure, should be accounted for when applying this method.

The computational approach for investigating the nanomechanical stability of the anticalin:CTLA-4 complex under different pulling directions was parametrized by tuning the interface energy. This rendered the Gō-MARTINI approach a very predictable model for the study of large conformational changes of protein complexes at much cheaper computational cost than in regular SMD

simulation allowing larger sampling of pathways. This model not only allowed the reproduction of the phenomenological one-to-one experimental SMFS profile for anticalin:CTLA-4 complex, but also unveiled microscopic pathways and mechanistic explanations of the higher mechanical stability observed when pulling anticalin at residue 60. Our computational study explained this stability in terms of translations of anticalin COM, and loss of NCs in anticalin. The simulations show that certain pulling directions can partially unfold the anticalin and destabilize the interface while other positions maintain the close contact of the proteins at the interface.

The anticalin against CTLA-4 shares very high structural similarity with other previously reported engineered anticalins (**Fig. S1**). In the future, it will be interesting to see if the mechanically optimal pulling point (residue 60) is generalizable to other anticalin:ligand complexes. Our research demonstrated that the mechanical stability of protein-ligand systems can be tuned by precisely controlling the loading geometry, without changing equilibrium binding properties. This suggests a new paradigm for affinity maturation of non-antibody scaffolds by correctly choosing the anchor points. Such an approach could be particularly beneficial for targeting therapeutic nanoparticles or imaging probes which can exert shear forces onto binding interfaces.

Acknowledgements

This work was supported by the University of Basel, ETH Zurich, an ERC Starting Grant (MMA-715207), the NCCR in Molecular Systems Engineering, and the Swiss National Science Foundation (Project 200021_175478). The authors thank Peter Schultz for providing the pEVOL-pAzF plasmid and Lloyd Ruddock for providing the pMJS205 plasmid. The authors thank Timothy Sharpe and the Biophysics Facility of Biozentrum, University of Basel for the help with affinity measurements using MST. A.B.P. acknowledges financial support from the National Science Centre, Poland, under grant No. 2017/26/D/NZ1/00466, also gratefully acknowledge the computing provided by the Jülich Supercomputing Centre on the supercomputer JURECA at Forschungszentrum Jülich and additional computer resources were supported by the PL-GRID infrastructure.

References

(1) Bedford, R.; Tiede, C.; Hughes, R.; Curd, A.; McPherson, M. J.; Peckham, M.; Tomlinson, D. C. Alternative Reagents to Antibodies in Imaging Applications. *Biophys. Rev.* **2017**, *9* (4), 299–308.
(2) Richards, D. A. Exploring Alternative Antibody Scaffolds: Antibody Fragments and Antibody Mimics for Targeted Drug Delivery. *Drug Discov. Today Technol.* **2018**, *30*, 35–46.
(3) Škrlec, K.; Štrukelj, B.; Berlec, A. Non-Immunoglobulin Scaffolds: A Focus on Their Targets. *Trends Biotechnol.* **2015**, *33* (7), 408–418.
(4) Rothe, C.; Skerra, A. Anticalin® Proteins as Therapeutic Agents in Human Diseases. *BioDrugs* **2018**, *32* (3), 233–243.
(5) Schönfeld, D.; Matschiner, G.; Chatwell, L.; Trentmann, S.; Gille, H.; Hülsmeyer, M.; Brown, N.; Kaye, P. M.; Schlehuber, S.; Hohlbaum, A. M.; Skerra, A. An Engineered Lipocalin Specific for CTLA-4 Reveals a Combining Site with Structural and Conformational Features Similar to Antibodies. *Proc. Natl. Acad. Sci. U. S. A.* **2009**, *106* (20), 8198–8203.
(6) Gille, H.; Hülsmeyer, M.; Trentmann, S.; Matschiner, G.; Christian, H. J.; Meyer, T.; Amirkhosravi, A.; Audoly, L. P.; Hohlbaum, A. M.; Skerra, A. Functional Characterization of a VEGF-A-Targeting Anticalin, Prototype of a Novel Therapeutic Human Protein Class. *Angiogenesis* **2016**, *19* (1), 79–94.
(7) Eggenstein, E.; Eichinger, A.; -J. Kim, H.; Skerra, A. Structure-Guided Engineering of Anticalins with Improved Binding Behavior and Biochemical Characteristics for Application in Radio-Immuno Imaging And/or Therapy. *Journal of Structural Biology*. 2014, pp 203–214. https://doi.org/10.1016/j.jsb.2013.03.009.
(8) Schiefner, A.; Gebauer, M.; Richter, A.; Skerra, A. Anticalins Reveal High Plasticity in the Mode of Complex Formation with a Common Tumor Antigen. *Structure* **2018**, *26* (4), 649–656.e3.
(9) Renders, L.; Budde, K.; Rosenberger, C.; van Swelm, R.; Swinkels, D.; Dellanna, F.; Feuerer, W.; Wen, M.; Erley, C.; Bader, B.; Sommerer, C.; Schaier, M.; Meurer, K.; Matis, L. First-in-Human Phase I Studies of PRS-080#22, a Hepcidin Antagonist, in Healthy Volunteers and Patients with Chronic Kidney Disease Undergoing Hemodialysis. *PLOS ONE*. 2019, p e0212023. https://doi.org/10.1371/journal.pone.0212023.
(10) Deuschle, F.-C.; Morath, V.; Schiefner, A.; Brandt, C.; Ballke, S.; Reder, S.; Steiger, K.; Schwaiger, M.; Weber, W.; Skerra, A. Development of a High Affinity Anticalin® Directed against Human CD98hc for Theranostic Applications. *Theranostics* **2020**, *10* (5), 2172–2187.
(11) Lee, K. M.; Chuang, E.; Griffin, M.; Khattri, R.; Hong, D. K.; Zhang, W.; Straus, D.; Samelson, L. E.; Thompson, C. B.; Bluestone, J. A. Molecular Basis of T Cell Inactivation by CTLA-4. *Science* **1998**, *282* (5397), 2263–2266.
(12) Walker, L. S. K.; Sansom, D. M. The Emerging Role of CTLA4 as a Cell-Extrinsic Regulator of T Cell Responses. *Nat. Rev. Immunol.* **2011**, *11* (12), 852–863.
(13) Egen, J. G.; Kuhns, M. S.; Allison, J. P. CTLA-4: New Insights into Its Biological Function and Use in Tumor Immunotherapy. *Nat. Immunol.* **2002**, *3* (7), 611–618.
(14) Sharma, P.; Allison, J. P. The Future of Immune Checkpoint Therapy. *Science* **2015**, *348* (6230), 56–61.
(15) Leach, D. R.; Krummel, M. F.; Allison, J. P. Enhancement of Antitumor Immunity by CTLA-4 Blockade. *Science* **1996**, *271* (5256), 1734–1736.
(16) Lipson, E. J.; Drake, C. G. Ipilimumab: An Anti-CTLA-4 Antibody for Metastatic Melanoma. *Clin. Cancer Res.* **2011**, *17* (22), 6958–6962.
(17) Khagi, Y.; Kurzrock, R.; Patel, S. P. Next Generation Predictive Biomarkers for Immune Checkpoint Inhibition. *Cancer Metastasis Rev.* **2017**, *36* (1), 179–190.
(18) Puri, A.; Kramer-Marek, G.; Campbell-Massa, R.; Yavlovich, A.; Tele, S. C.; Lee, S.-B.; Clogston, J. D.; Patri, A. K.; Blumenthal, R.; Capala, J. HER2-Specific Affibody-Conjugated Thermosensitive Liposomes (Affisomes) for Improved Delivery of Anticancer Agents. *J. Liposome Res.* **2008**, *18* (4), 293–307.
(19) Shishido, T.; Mieda, H.; Hwang, S. Y.; Nishimura, Y.; Tanaka, T.; Ogino, C.; Fukuda, H.; Kondo, A. Affibody-Displaying Bionanocapsules for Specific Drug Delivery to HER2-

Expressing Cancer Cells. *Bioorg. Med. Chem. Lett.* **2010**, *20* (19), 5726–5731.
(20) Lee, J.-J.; Kang, J. A.; Ryu, Y.; Han, S.-S.; Nam, Y. R.; Rho, J. K.; Choi, D. S.; Kang, S.-W.; Lee, D.-E.; Kim, H.-S. Genetically Engineered and Self-Assembled Oncolytic Protein Nanoparticles for Targeted Cancer Therapy. *Biomaterials* **2017**, *120*, 22–31.
(21) Dietz, H.; Berkemeier, F.; Bertz, M.; Rief, M. Anisotropic Deformation Response of Single Protein Molecules. *Proc. Natl. Acad. Sci. U. S. A.* **2006**, *103* (34), 12724–12728.
(22) Carrion-Vazquez, M.; Li, H.; Lu, H.; Marszalek, P. E.; Oberhauser, A. F.; Fernandez, J. M. The Mechanical Stability of Ubiquitin Is Linkage Dependent. *Nat. Struct. Biol.* **2003**, *10* (9), 738–743.
(23) Brockwell, D. J.; Paci, E.; Zinober, R. C.; Beddard, G. S.; Olmsted, P. D.; Smith, D. A.; Perham, R. N.; Radford, S. E. Pulling Geometry Defines the Mechanical Resistance of a β-Sheet Protein. *Nat. Struct. Mol. Biol.* **2003**, *10* (9), 731–737.
(24) Li, Y. D.; Lamour, G.; Gsponer, J.; Zheng, P.; Li, H. The Molecular Mechanism Underlying Mechanical Anisotropy of the Protein GB1. *Biophys. J.* **2012**, *103* (11), 2361–2368.
(25) Schoeler, C.; Bernardi, R. C.; Malinowska, K. H.; Durner, E.; Ott, W.; Bayer, E. A.; Schulten, K.; Nash, M. A.; Gaub, H. E. Mapping Mechanical Force Propagation through Biomolecular Complexes. *Nano Lett.* **2015**, *15* (11), 7370–7376.
(26) Sedlak, S. M.; Schendel, L. C.; Melo, M. C. R.; Pippig, D. A.; Luthey-Schulten, Z.; Gaub, H. E.; Bernardi, R. C. Direction Matters: Monovalent Streptavidin/Biotin Complex under Load. *Nano Lett.* **2019**, *19* (6), 3415–3421.
(27) Sedlak, S. M.; Schendel, L. C.; Gaub, H. E.; Bernardi, R. C. Streptavidin/biotin: Tethering Geometry Defines Unbinding Mechanics. *Sci Adv* **2020**, *6* (13), eaay5999.
(28) Ott, W.; Jobst, M. A.; Schoeler, C.; Gaub, H. E.; Nash, M. A. Single-Molecule Force Spectroscopy on Polyproteins and Receptor–ligand Complexes: The Current Toolbox. *J. Struct. Biol.* **2017**, *197* (1), 3–12.
(29) Sedlak, S. M.; Bauer, M. S.; Kluger, C.; Schendel, L. C.; Milles, L. F.; Pippig, D. A.; Gaub, H. E. Monodisperse Measurement of the Biotin-Streptavidin Interaction Strength in a Well-Defined Pulling Geometry. *PLoS One* **2017**, *12* (12), e0188722.
(30) Yang, B.; Liu, Z.; Liu, H.; Nash, M. A. Next Generation Methods for Single-Molecule Force Spectroscopy on Polyproteins and Receptor-Ligand Complexes. *Front Mol Biosci* **2020**, *7*, 85.
(31) Goetz, D. H.; Holmes, M. A.; Borregaard, N.; Bluhm, M. E.; Raymond, K. N.; Strong, R. K. The Neutrophil Lipocalin NGAL Is a Bacteriostatic Agent That Interferes with Siderophore-Mediated Iron Acquisition. *Mol. Cell* **2002**, *10* (5), 1033–1043.
(32) Gebauer, M.; Schiefner, A.; Matschiner, G.; Skerra, A. Combinatorial Design of an Anticalin Directed against the Extra-Domain B for the Specific Targeting of Oncofetal Fibronectin. *J. Mol. Biol.* **2013**, *425* (4), 780–802.
(33) Korndörfer, I. P.; Beste, G.; Skerra, A. Crystallographic Analysis of an "Anticalin" with Tailored Specificity for Fluorescein Reveals High Structural Plasticity of the Lipocalin Loop Region. *Proteins* **2003**, *53* (1), 121–129.
(34) Breustedt, D. A.; Chatwell, L.; Skerra, A. A New Crystal Form of Human Tear Lipocalin Reveals High Flexibility in the Loop Region and Induced Fit in the Ligand Cavity. *Acta Crystallogr. D Biol. Crystallogr.* **2009**, *65* (10), 1118–1125.
(35) Flower, D. R. The Lipocalin Protein Family: Structure and Function. *Biochem. J* **1996**, *318 (Pt 1)*, 1–14.
(36) Coles, M.; Diercks, T.; Muehlenweg, B.; Bartsch, S.; Zölzer, V.; Tschesche, H.; Kessler, H. The Solution Structure and Dynamics of Human Neutrophil Gelatinase-Associated Lipocalin. *J. Mol. Biol.* **1999**, *289* (1), 139–157.
(37) Chin, J. W.; Santoro, S. W.; Martin, A. B.; King, D. S.; Wang, L.; Schultz, P. G. Addition of P-Azido-L-Phenylalanine to the Genetic Code of Escherichia Coli. *J. Am. Chem. Soc.* **2002**, *124* (31), 9026–9027.
(38) Debets, M. F.; van Berkel, S. S.; Schoffelen, S.; Rutjes, F. P. J. T.; van Hest, J. C. M.; van Delft, F. L. Aza-Dibenzocyclooctynes for Fast and Efficient Enzyme PEGylation via Copper-Free (3+2) Cycloaddition. *Chem. Commun.* **2010**, *46* (1), 97–99.
(39) Schwaiger, I.; Kardinal, A.; Schleicher, M.; Noegel, A. A.; Rief, M. A Mechanical Unfolding Intermediate in an Actin-Crosslinking Protein. *Nat. Struct. Mol. Biol.* **2004**, *11* (1), 81–85.

(40) Yin, J.; Straight, P. D.; McLoughlin, S. M.; Zhou, Z.; Lin, A. J.; Golan, D. E.; Kelleher, N. L.; Kolter, R.; Walsh, C. T. Genetically Encoded Short Peptide Tag for Versatile Protein Labeling by Sfp Phosphopantetheinyl Transferase. *Proc. Natl. Acad. Sci. U. S. A.* **2005**, *102* (44), 15815–15820.
(41) Milles, L. F.; Schulten, K.; Gaub, H. E.; Bernardi, R. C. Molecular Mechanism of Extreme Mechanostability in a Pathogen Adhesin. *Science* **2018**.
(42) Ponnuraj, K.; Bowden, M. G.; Davis, S.; Gurusiddappa, S.; Moore, D.; Choe, D.; Xu, Y.; Hook, M.; Narayana, S. V. L. A "dock, Lock, and Latch" Structural Model for a Staphylococcal Adhesin Binding to Fibrinogen. *Cell* **2003**, *115* (2), 217–228.
(43) Livadaru, L.; Netz, R. R.; Kreuzer, H. J. Stretching Response of Discrete Semiflexible Polymers. *Macromolecules* **2003**, *36* (10), 3732–3744.
(44) Puchner, E. M.; Franzen, G.; Gautel, M.; Gaub, H. E. Comparing Proteins by Their Unfolding Pattern. *Biophys. J.* **2008**, *95* (1), 426–434.
(45) Jobst, M. A.; Schoeler, C.; Malinowska, K.; Nash, M. A. Investigating Receptor-Ligand Systems of the Cellulosome with AFM-Based Single-Molecule Force Spectroscopy. *J. Vis. Exp.* **2013**, No. 82, e50950.
(46) Bell, G. I. Models for the Specific Adhesion of Cells to Cells. *Science* **1978**, *200* (4342), 618–627.
(47) Evans, E.; Ritchie, K. Dynamic Strength of Molecular Adhesion Bonds. *Biophys. J.* **1997**.
(48) Dudko, O. K.; Hummer, G.; Szabo, A. Intrinsic Rates and Activation Free Energies from Single-Molecule Pulling Experiments. *Phys. Rev. Lett.* **2006**, *96* (10), 108101.
(49) Dudko, O. K.; Hummer, G.; Szabo, A. Theory, Analysis, and Interpretation of Single-Molecule Force Spectroscopy Experiments. *Proc. Natl. Acad. Sci. U. S. A.* **2008**, *105* (41), 15755–15760.
(50) Atilgan, A. R.; Durell, S. R.; Jernigan, R. L.; Demirel, M. C.; Keskin, O.; Bahar, I. Anisotropy of Fluctuation Dynamics of Proteins with an Elastic Network Model. *Biophys. J.* **2001**, *80* (1), 505–515.
(51) Eyal, E.; Lum, G.; Bahar, I. The Anisotropic Network Model Web Server at 2015 (ANM 2.0). *Bioinformatics* **2015**, *31* (9), 1487–1489.
(52) Doruker, P.; Atilgan, A. R.; Bahar, I. Dynamics of Proteins Predicted by Molecular Dynamics Simulations and Analytical Approaches: Application to α-Amylase Inhibitor. *Proteins: Struct. Funct. Bioinf.* **2000**, *40* (3), 512–524.
(53) Eyal, E.; Bahar, I. Toward a Molecular Understanding of the Anisotropic Response of Proteins to External Forces: Insights from Elastic Network Models. *Biophys. J.* **2008**, *94* (9), 3424–3435.
(54) Souza, P. C. T.; Thallmair, S.; Conflitti, P.; Ramírez-Palacios, C.; Alessandri, R.; Raniolo, S.; Limongelli, V.; Marrink, S. J. Protein-Ligand Binding with the Coarse-Grained Martini Model. *Nat. Commun.* **2020**, *11* (1), 3714.
(55) Souza, P. C. T.; Alessandri, R.; Barnoud, J.; Thallmair, S.; Faustino, I.; Grunewald, F.; Patmanidis, I.; Abdizadeh, H.; Bruininks, B. M. H.; Wassenaar, T. A.; Kroon, P. C.; Melcr, J.; Nieto, V.; Corradi, V.; Khan, H. M.; Domański, J.; Javanainen, M.; Martinez-Seara, H.; Reuter, N.; Best, R. B.; Vattulainen, I.; Monticelli, L.; Periole, X.; Peter Tieleman, D.; de Vries, A. H.; Marrink, S. J. Martini 3: A General Purpose Force Field for Coarse-Grain Molecular Dynamics. *Nat. Methods* **2021**, *in press*. https://doi.org/10.1038/s41592-021-01098-3.
(56) Poma, A. B.; Li, M. S.; Theodorakis, P. E. Generalization of the Elastic Network Model for the Study of Large Conformational Changes in Biomolecules. *Physical Chemistry Chemical Physics*. 2018, pp 17020–17028. https://doi.org/10.1039/c8cp03086c.
(57) Chwastyk, M.; Bernaola, A. P.; Cieplak, M. Statistical Radii Associated with Amino Acids to Determine the Contact Map: Fixing the Structure of a Type I Cohesin Domain in the Clostridium Thermocellum Cellulosome. *Phys. Biol.* **2015**, *12* (4), 046002.
(58) Senapati, S.; Poma, A. B.; Cieplak, M.; Filipek, S.; Park, P. S. H. Differentiating between Inactive and Active States of Rhodopsin by Atomic Force Microscopy in Native Membranes. *Anal. Chem.* **2019**, *91* (11), 7226–7235.
(59) Poma, A. B.; Chwastyk, M.; Cieplak, M. Elastic Moduli of Biological Fibers in a Coarse-Grained Model: Crystalline Cellulose and β-Amyloids. *Phys. Chem. Chem. Phys.* **2017**, *19* (41), 28195–28206.
(60) Moreira, R. A.; Chwastyk, M.; Baker, J. L.; Guzman, H. V.; Poma, A. B. Quantitative

Determination of Mechanical Stability in the Novel Coronavirus Spike Protein. *Nanoscale* **2020**, *12* (31), 16409–16413.
(61) Poma, A. B.; Guzman, H. V.; Li, M. S.; Theodorakis, P. E. Mechanical and Thermodynamic Properties of Aβ42, Aβ40, and α-Synuclein Fibrils: A Coarse-Grained Method to Complement Experimental Studies. *Beilstein J. Nanotechnol.* **2019**, *10*, 500–513.
(62) Poma, A. B.; Cieplak, M.; Theodorakis, P. E. Combining the MARTINI and Structure-Based Coarse-Grained Approaches for the Molecular Dynamics Studies of Conformational Transitions in Proteins. *J. Chem. Theory Comput.* **2017**, *13* (3), 1366–1374.
(63) Fontana, F.; Gelain, F. Probing Mechanical Properties and Failure Mechanisms of Fibrils of Self-Assembling Peptides. *Nanoscale Advances* **2020**, *2* (1), 190–198.
(64) Alessandri, R.; Souza, P. C. T.; Thallmair, S.; Melo, M. N.; de Vries, A. H.; Marrink, S. J. Pitfalls of the Martini Model. *J. Chem. Theory Comput.* **2019**, *15* (10), 5448–5460.